Available online at www.sciencedirect.com
SCIENCE DIRECT®
Astroparticle Physics 22 (2005) 339–353
Astroparticle Physics
www.elsevier.com/locate/astropart

Flux limits on ultra high energy neutrinos with AMANDA-B10

M. Ackermann [a], J. Ahrens [b], H. Albrecht [a], D. Atlee [c], X. Bai [d], R. Bay [e], M. Bartelt [f], S.W. Barwick [g], T. Becka [b], K.H. Becker [f], J.K. Becker [f], E. Bernardini [a], D. Bertrand [h], D.J. Boersma [a], S. Böser [a], O. Botner [i], A. Bouchta [i], O. Bouhali [h], J. Braun [j], C. Burgess [k], T. Burgess [k], T. Castermans [l], D. Chirkin [e], T. Coarasa [c], B. Collin [c], J. Conrad [i], J. Cooley [j], D.F. Cowen [c], A. Davour [i], C. De Clercq [m], T. DeYoung [n], P. Desiati [j], P. Ekström [k], T. Feser [b], T.K. Gaisser [d], R. Ganugapati [j], H. Geenen [f], L. Gerhardt [g], A. Goldschmidt [o], A. Groß [f], A. Hallgren [i], F. Halzen [j], K. Hanson [j], D. Hardtke [e], R. Hardtke [j], T. Harenberg [f], T. Hauschildt [a], K. Helbing [o], M. Hellwig [b], P. Herquet [l], G.C. Hill [j], J. Hodges [j], D. Hubert [m], B. Hughey [j], P.O. Hulth [k], K. Hultqvist [k], S. Hundertmark [k,*], J. Jacobsen [o], K.H. Kampert [f], A. Karle [j], J. Kelley [j], M. Kestel [c], L. Köpke [b], M. Kowalski [a], M. Krasberg [j], K. Kuehn [g], H. Leich [a], M. Leuthold [a], J. Lundberg [i], J. Madsen [p], K. Mandli [j], P. Marciniewski [i], H.S. Matis [o], C.P. McParland [o], T. Messarius [f], Y. Minaeva [k], P. Miočinović [e], R. Morse [j], S. Movit [c], K. Münich [f], R. Nahnhauer [a], J.W. Nam [g], T. Neunhöffer [b], P. Niessen [d], D.R. Nygren [o], H. Ögelman [j], Ph. Olbrechts [m], C. Pérez de los Heros [i], A.C. Pohl [q], R. Porrata [e], P.B. Price [e], G.T. Przybylski [o], K. Rawlins [j], E. Resconi [a], W. Rhode [f], M. Ribordy [l], S. Richter [j], J. Rodríguez Martino [k], D. Rutledge [c], H.G. Sander [b], K. Schinarakis [f], S. Schlenstedt [a], D. Schneider [j], R. Schwarz [j], A. Silvestri [g], M. Solarz [e], G.M. Spiczak [p], C. Spiering [a], M. Stamatikos [j], D. Steele [j], P. Steffen [a], R.G. Stokstad [o], K.H. Sulanke [a], I. Taboada [r], O. Tarasova [a], L. Thollander [k], S. Tilav [d], L.C. Voicu [c], W. Wagner [f], C. Walck [k], M. Walter [a], Y.R. Wang [j], C.H. Wiebusch [f], R. Wischnewski [a], H. Wissing [a], K. Woschnagg [e], G. Yodh [g]

[*] Corresponding author.
E-mail address: stephan.hundertmark@physto.se (S. Hundertmark).

0927-6505/$ - see front matter
doi:10.1016/j.astropartphys.2004.09.008

[a] DESY, 15735 Zeuthen, Germany
[b] Institute of Physics, University of Mainz, D-55099 Mainz, Germany
[c] Department of Physics, Pennsylvania State University, University Park, PA 16802, USA
[d] Bartol Research Institute, University of Delaware, Newark, DE 19716, USA
[e] Department of Physics, University of California, Berkeley, CA 94720, USA
[f] Department of Physics, Bergische Univerität Wuppertal, 42097 Wuppertal, Germany
[g] Department of Physics and Astronomy, University of California, Irvine, CA 92697, USA
[h] Université Libre de Bruxelles, Science Faculty CP230, Boulevard du Triomphe, B-1050 Brussels, Belgium
[i] Division of High Energy Physics, Uppsala University, S-75121 Uppsala, Sweden
[j] Department of Physics, University of Wisconsin, Madison, WI 53706, USA
[k] Department of Physics, Stockholm University, SE-10691 Stockholm, Sweden
[l] University of Mons-Hainaut, 7000 Mons, Belgium
[m] Vrije Universiteit Brussel, Dienst ELEM, B-1050 Brussels, Belgium
[n] Department of Physics, University of Maryland, College Park, MD 20742, USA
[o] Lawrence Berkeley National Laboratory, Berkeley, CA 94720, USA
[p] Physics Department, University of Wisconsin, River Falls, WI 54022, USA
[q] Department of Chemistry and Biomedical Sciences, University of Kalmar, S-39182 Kalmar, Sweden
[r] Department of Physics, Universidad Simón Bolívar, Caracas, 1080, Venezuela

Received 17 August 2004; received in revised form 22 September 2004; accepted 30 September 2004
Available online 13 November 2004

Abstract

Data taken during 1997 with the AMANDA-B10 detector are searched for a diffuse flux of neutrinos of all flavors with energies above 10^{16} eV. At these energies the Earth is opaque to neutrinos, and thus neutrino induced events are concentrated at the horizon. The background are large muon bundles from down-going atmospheric air shower events. No excess events above the background expectation are observed and a neutrino flux following E^{-2}, with an equal mix of all flavors, is limited to $E^2\Phi(10^{15}\,\mathrm{eV} < E < 3\times10^{18}\,\mathrm{eV}) \leqslant 0.99\times10^{-6}\,\mathrm{GeV\,cm^{-2}\,s^{-1}\,sr^{-1}}$ at 90% confidence level. This is the most restrictive experimental bound placed by any neutrino detector at these energies. Bounds to specific extra-terrestrial neutrino flux predictions are also presented.

PACS: 95.55.Vj; 95.85.Ry; 96.40.Tv
Keywords: Neutrino telescopes; Neutrino astronomy; UHE neutrinos; AMANDA

1. Introduction

Neutrino telescopes like AMANDA [1] are unique astronomy tools, originally designed to look downwards for Cherenkov light emitted by upward traveling muons from charged-current muon–neutrino interactions. The Earth is used to filter the muon flux from cosmic ray air showers. As muons cannot pass through the Earth, any upward traveling muon in the vicinity of the detector is neutrino induced. Due to the sparse instrumentation of the detection medium and the optical properties of the medium itself, misidentification of the direction of the muon by the reconstruction algorithm is possible. To reduce the amount of down-going muons, and therefore the probability for misidentification, these detectors are located under as much overburden as feasible.

As the energy of the neutrino increases, the neutrino–nucleon cross section and the muon range grow. Both effects result in a large detection probability for high energy neutrinos. Above 40 TeV, the Earth diameter exceeds the neutrino charged-current interaction length and high energy neutri-

nos are significantly absorbed [2]. At UHE [1] the Earth is essentially opaque to muon- and electron–neutrinos [3] and only downward to horizontally traveling neutrinos can be detected. The overburden above the AMANDA detector is limited, which limits the interaction probability for neutrinos, concentrating the muons from UHE neutrinos at the horizon. Klein and Mann [3] estimate that a few muons per year above 10^{15} eV from UHE neutrino sources might be detected with an 0.1 km^2 detector, an effective area that is achieved by this analysis (as shown in [4]). The energy range above 10^{16} eV is interesting, as experimentally there are currently no strong limits on neutrino fluxes from models describing active galactic nuclei (AGN) at these energies. At higher energies, above 10^{18} eV, one expects the guaranteed flux of neutrinos from interactions of high energy cosmic rays with the cosmic microwave background, or the more speculative flux from decays of topological defects (for an overview see [5–7]). Cosmological sources are expected to produce neutrinos in pp or pγ collisions, resulting in a flavor ratio of $\nu_e:\nu_\mu:\nu_\tau = 1:2:0$ at the source. As these neutrinos propagate over cosmological distances, oscillations between the different flavors result in a ratio at Earth of $\nu_e:\nu_\mu:\nu_\tau = 1:1:1$ [8]. Therefore all three flavors are initially of the same importance for detection, but for muon–neutrinos the detection probability is higher, due to the long path length of the resulting muons.

The search for a neutrino signal in the upper hemisphere has to be performed in the presence of the large flux of down-going atmospheric muon bundles. This analysis exploits the fact that these events have different characteristics than neutrino induced events. The primary cosmic ray spectrum (protons and heavier elements) falls rapidly with energy, following approximately $E^{-2.7}$ below the knee and steepening thereafter to $E^{-3.1}$. An atmospheric air shower produced by an UHE primary particle results in a muon bundle consisting of hundreds to thousands of muons. At 10^{16}–10^{20} eV approximately 90% of the primary energy is consumed by the electromagnetic cascade of the air shower and only a fraction of the remaining energy is carried by the resulting muons [9]. When comparing a single muon and a muon bundle of the same energy, the bundle spreads the generated Cherenkov light over a larger volume. In the detector, both classes of events can result in a large number of photomultiplier tubes (PMT) being hit by photons, but neutrino induced events have more photon hits overall, i.e. more multiple hits are found in single PMTs. Often, however, single photons cannot be resolved. This can be compensated for by exploiting the afterpulse behavior of the PMTs. Each photoelectron has a small probability to generate an afterpulse delayed by several microseconds. These afterpulses are used as a "low gain" outlet to identify high energy events with a large number of photons incident on the PMT. Using this and other event properties, it is possible to reduce the number of events caused by down-going atmospheric muons to a level where a search for a signal from UHE neutrinos becomes feasible. In [4] and [10] part of the data taken in 1997 with the AMANDA-B10 array was used to establish this technique and a preliminary limit was set. In this analysis an improved neutrino simulation is used, selection criteria are refined, systematic uncertainties are assessed and the analysis is applied to the full 1997 data set.

2. The AMANDA-B10 detector

The data used in this analysis were taken with the AMANDA-B10 detector [1] in 1997. This detector consists of 302 Optical Modules (OMs) on 10 vertical strings. The instrumented parts of the strings are located between 1500 m and 2000 m below the South Pole ice surface. The strings are arranged in two concentric circles. The outer circle with a diameter of 120 m is formed by six strings equipped with a total of 216 OMs connected to the surface via twisted pair cables. The vertical separation of the OMs located on these strings is 10 m. Three strings lie on a 60 m diameter inner circle, the remaining string being located at the center. These strings use coaxial cable to connect 86 OMs, with 20 m spacing, to the surface. The coaxial or twisted pair cable

[1] *U*ltra *H*igh *E*nergy is used here for energies above 10^{16} eV.

supplies the PMT inside the OM-pressure-sphere with high voltage power and transmits the signal to the amplifier and data acquisition electronics (DAQ) located at the surface. The electrical signal from the PMT is dispersed in the cable, which strongly limits the capability to resolve single photons arriving at the PMT separated by less than a few hundred nanoseconds. The PMT and/or the amplifier saturate when more than some tens of photoelectrons are generated in the PMT. Each photoelectron produces an afterpulse with an approximately 3% probability, well separated by approximately 6 μs from the initial pulse. These late afterpulses appear when residual gas molecules, ionized by electrons from the electron multiplier, travel back to the cathode and release additional electrons [11,12]. The AMANDA-B10 detector and its response to a simulated horizontal 2×10^{19} eV muon is shown in Fig. 1.

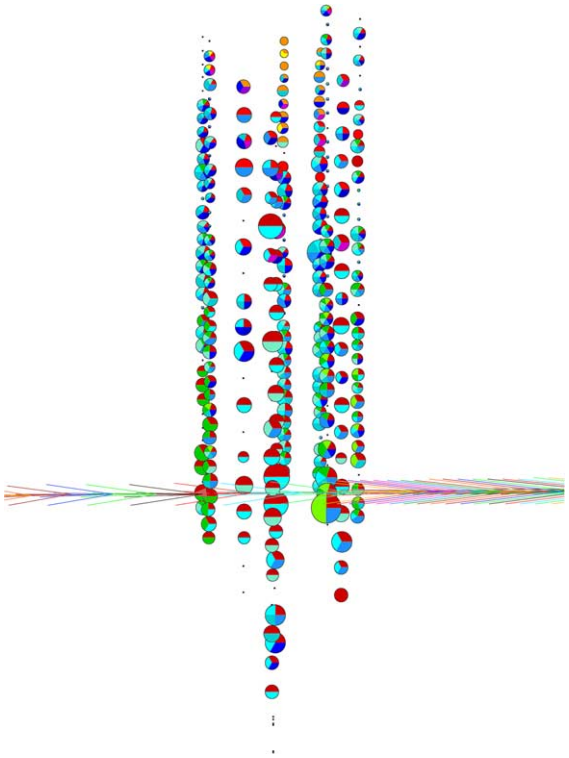

Fig. 1. A simulated horizontal 2×10^{19} eV muon passes the AMANDA-B10 detector. The different colors of the OMs correspond to different hit times from yellow (early) to blue (late). Only the hits depicted in yellow, orange and red are generated by the muon, while the green and blue colored hits are caused by afterpulses. In this event, all working OMs are hit and nearly all of them report at least one hit from afterpulsing. (For interpretation of the references in color in this figure legend, the reader is referred to the web version of this article.)

3. Signal and background simulations

3.1. UHE neutrino simulation

The neutrino generator ANIS [13] is used to generate neutrinos and anti-neutrinos of all flavors following an E^{-1} spectrum between 10^{13} eV and 10^{20} eV. All relevant standard model processes, like charged- and neutral-current νN interactions, resonant $\overline{\nu}_e e^-$ scattering and tau–neutrino regeneration are simulated. Cross-sections are evaluated up to 10^{21} eV following the framework of pQCD and with structure functions according to CTEQ5. The neutrinos are propagated through the Earth with a density profile taken from the Preliminary Reference Earth Model [14]. In case of a charged-current interaction in the vicinity of the detector, the resulting lepton and hadronic energy deposition is simulated. Throughout this paper a neutrino flavor ratio at Earth of $\nu_e:\nu_\mu:\nu_\tau = 1:1:1$ and a ratio of $\nu/\overline{\nu} = 1$ [2] is assumed. The events, generated by ANIS, are re-weighted to a diffuse AGN-like flux $E^2\Phi = 10^{-6}\,\mathrm{GeV\,cm^{-2}\,s^{-1}\,sr^{-1}}$ or other UHE neutrino flux predictions. Fig. 2 shows the zenith angle distribution for muon–neutrinos which underwent a charged-current interaction within the muon path length from the detector. With increasing neutrino energy, the absorption of the neutrino flux becomes stronger and the resulting muon flux concentrates near the horizon. The event selection is developed using a simpler single muon simulation, re-weighted to an E^{-2} neutrino spectrum. In this simulation the Earth is assumed to have the density of ice and the hadronic energy deposition from the charged-current interaction is neglected. Nevertheless, this simplified simulation leads to a good agreement in the

[2] The production of high energy $\overline{\nu_e}$ is suppressed in $p\gamma \to n\pi^+$ interactions, altering the ratio $\nu/\overline{\nu}$. For a discussion of this effect see [35].

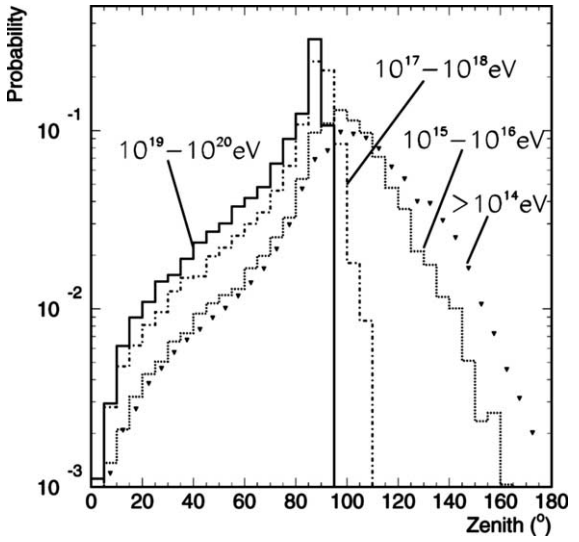

Fig. 2. Zenith angle distribution for muon–neutrinos which produced a muon able to reach the detector (A zenith angle of 180° corresponds to a upward-going particle). The probability distribution is shown for a muon–neutrino flux following E^{-2} and energies above 10^{14} eV and between 10^{15}–10^{16} eV, 10^{17}–10^{18} eV and 10^{19}–10^{20} eV.

final neutrino energy and angular distributions when compared to the results using the ANIS generator.

3.2. Cosmic ray air shower generation

Cosmic ray air showers are generated using the CORSIKA program (version 5.7001, 1988) [15] with the QGSJET interaction model. To develop the selection criteria, two sets of simulations are performed. The first uses the primary composition and the spectral slopes for the individual elements from [16], with energies of the primary particles ranging from 8×10^{11} eV to 10^{20} eV. This simulation corresponds to the standard AMANDA background simulation. The second set is tailored to more efficiently simulate events generated by high energy primaries. Protons and iron primaries are sampled from an E^{-2} spectrum from 8×10^{13} eV to 10^{20} eV. Events resulting from 315×10^{6} proton- and 145×10^{6} iron-primaries are re-weighted to the model taken from [17], which is shown in Fig. 3. This model describes

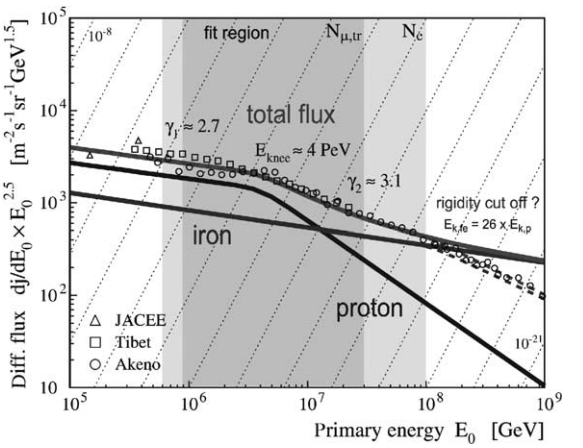

Fig. 3. The two-component model describing the averaged measured primary cosmic ray flux taken from [17] is used to simulate the cosmic ray air shower events.

the averaged measured primary cosmic ray flux with proton and iron primaries. As the developed selection criteria reject events generated by low energy primaries, the higher energy threshold and the softer spectral slope allows to reduce the required cpu time while generating a large number of high energy air shower events.

3.3. Lepton propagation

Muons and taus produced in charged-current neutrino interactions are propagated through the ice and rock using MMC [18] while for muons generated in cosmic ray air showers an algorithm developed by Lipari and Stanev [19] is used. The simulation takes into account the response of the detector to additional Cherenkov photons generated by energy depositions due to ionization and radiative processes. Table 1 shows the mean path length of muons in ice as evaluated with the algorithm presented in [19]. At

Table 1
The mean path length for muons ($\langle L_\mu \rangle$) with energies from 10^{15} eV to 10^{20} eV

E_μ (eV)	10^{15}	10^{16}	10^{17}	10^{18}	10^{19}	10^{20}
$\langle L_\mu \rangle$(kmwe)	17	21	26	30	33	37

UHE energies, muons can travel up to several tens of kilometers, which allows to monitor large volumes of ice.

4. Data selection and analysis

During the 1997 data taking period a total of 1.05×10^9 events satisfied a majority trigger of at least 16 hit OMs within about 2 μs. The data taking rate was 100 Hz. Out of the 302 OMs, 41 (14%) were either not functioning or showed abnormal behavior and were excluded from the analysis. Signals with a short time over threshold (TOT) are mostly caused by electrical cross talk between OMs on the same string and are removed from the analysis. In order to enhance high energy events, events that deposited a large amount of photons in and around the detector are selected by requiring hits in more than 95 OMs, with four of them located on the inner strings. During the detector's operational time of 174 days, 4×10^6 events fulfilling these criteria were collected. Taking into account the detector dead time of 25% the data taking period corresponds to 131 days of live time. The goal of this analysis is to reject atmospheric air shower events and retain a maximum number of UHE neutrino induced events. Due to the long path length of UHE muons (see Table 1), it is expected that events caused by muon–neutrinos contribute a larger fraction to the final event sample than electron– or tau–neutrino induced events. The development of selection criteria is therefore performed with simulated muon–neutrino induced events and only for the optimization of the final criterion the electron– and tau–neutrino induced events are added to the analysis.

4.1. Variables

To separate UHE neutrino induced signal events from air shower induced background events eight variables are used. Two neural nets (NN) combine subsets of these variables to achieve better separation. The variables are defined as follows:

1.	NCH	Number of hit OMs
2.	NHITS	Number of hits for all OMs
3.	F1H	Fraction of hit OMs with exactly one hit
4.	MA	Mean amplitude for hit OMs
5.	θ(FG)	Zenith angle obtained from first guess
6.	θ(LR)	Zenith angle obtained from likelihood reconstruction
7.	L	Likelihood for likelihood reconstruction
8.	S	Smallest moment of tensor of inertia

NCH is the number of OMs that reported one or more hits. The time-to-digital converters connected to each OM can distinguish up to eight hits. The variable NHITS is the sum of all hits for all OMs. Fig. 4(left) shows the NHITS distribution of the experiment, air shower and signal simulations. The atmospheric air shower simulation describes the experimental data well, while the signal simulation extends to larger values of NHITS. For bright events with many photons arriving at the OM, dispersion of the electrical signal in the cables to the surface effectively merges signals from primarily unscattered or only slightly scattered photons. F1H is the fraction of hit OMs with exactly one hit, divided by NCH. A faint signal induces mostly single photoelectrons in each hit OM and F1H is close to one, while bright events induce many photoelectrons per OM and therefore more afterpulses, both effects resulting in F1H closer to zero. This variable is therefore effective in selecting bright events. Fig. 4(right) shows F1H for experimental data and simulated signal and background. The air shower simulations describe the experimental data and the simulated signal events populate lower values of F1H. The mean amplitude per hit OM, MA, is the sum of amplitudes in hit OMs divided by NCH. Bright events have, on average, a higher mean amplitude. The first guess reconstruction (FG) and likelihood reconstruction (LR) return directional information. The quality of the likelihood reconstruction is reflected in the likelihood L. The underlying model for the likelihood reconstruction is a mini-

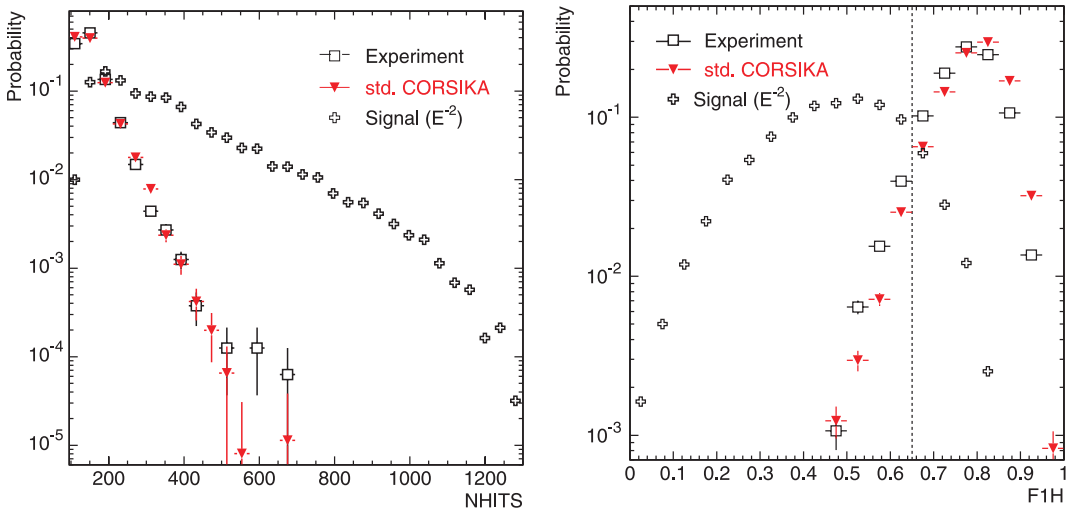

Fig. 4. The NHITS distributions for the experiment, air shower and signal simulation to the left and to the right F1H. At F1H = 0.65 the position of the selection criteria leading to the next level is shown.

mal ionizing muon that induces a comparatively small amount of Cherenkov light in the detector medium, while the first guess assumes light traveling at a certain speed along a line [3]. At high energies each OM receives hundreds to thousands of photons, significantly altering the arrival time probability as a function of distance. This leads to a poor resolution in the directional reconstruction for UHE events. Using the tensor of inertia for the events, the different shapes of the air shower and UHE neutrino induced events can be used. From the available variables the smallest eigenvalue of the tensor of inertia S shows the best discrimination power.

4.2. Level 1

Selecting events with F1H < 0.65 defines the Level 1 in this analysis. The experimental data sample is reduced to 263,000 events, or 6.5% of the initial sample. These events are reconstructed with the first guess and the likelihood reconstruction. The reconstructed zenith angles $(\theta(\mathrm{FG}), \theta(\mathrm{LR}))$, the likelihood parameter L and the F1H variable are used in the neural net NN1 to distinguish simulated signal from background. The simulation of air shower events gives reasonable agreement in the zenith angle distribution, for both first guess and likelihood reconstructions (Fig. 5). The distributions show that the reconstructions are not able to resolve the directional information of the UHE neutrino induced events, which are predominantly horizontal. Nevertheless, the direction of air shower muon events is better reconstructed and this is exploited by the neural net NN1. Fig. 6 shows the neural net output for experimental data, signal Monte Carlo and the two sets of air shower simulations. Both samples, the standard set of CORSIKA generated data with a limited amount of events (the outlier at NN1 ≈ 0.95 corresponds to one event) and the re-weighted high energy CORSIKA sample using only proton and iron cosmic ray primaries, show good agreement with the experimental data.

4.3. Level 2

Reducing the Monte-Carlo background to approximately 1% of the previous level, Level 2 is defined by selecting events with NN1 > 0.37. The experimental data set is reduced to 3326 events, while the air shower simulation predicts 2976 ± 51 events. This is 11% lower and within the systematic

[3] For more details on the reconstruction methods used in AMANDA see [20].

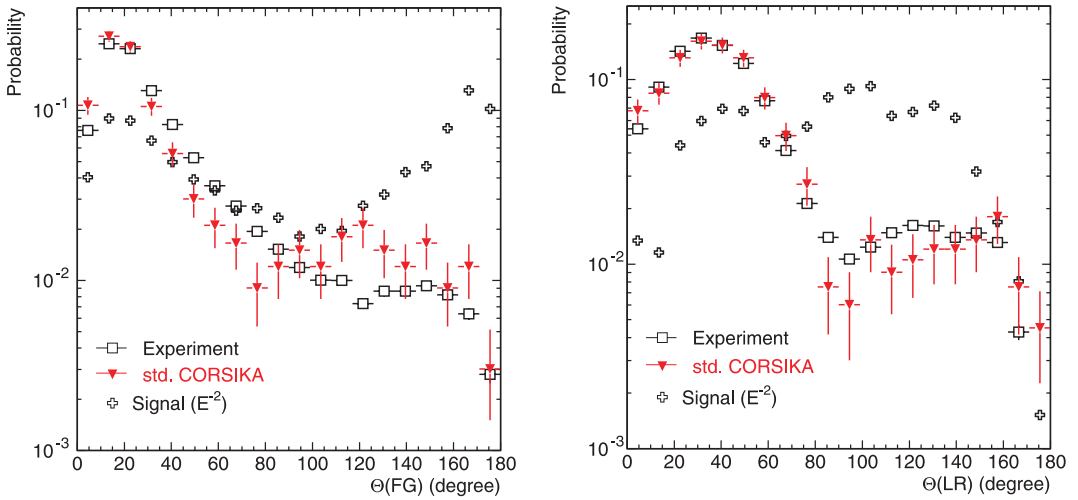

Fig. 5. The zenith angle distribution for the first guess (FG) (left) and the likelihood reconstruction (LR) (right).

uncertainty, as discussed later. At this level, the final selection criterion is defined, based on a second neural net (NN2) using the variables F1H, NCH, NHITS, MA and *S*. Other variables and combinations have been investigated, but the ones used are found to be the most effective. Fig. 7 shows the NN2 output for the experiment, the air shower and the combined electron–, muon– and tau–neutrino simulation. A Kolmogorov test, using the CORSIKA generated events and the experimental data yields a probability close to one for both cases resulting from the same parent distribution.

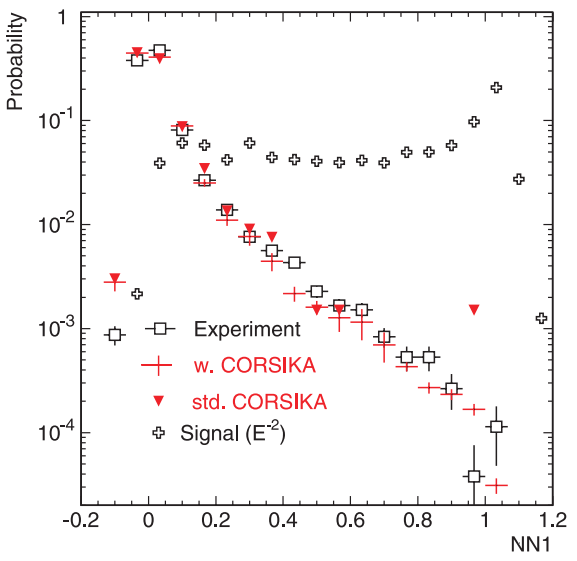

Fig. 6. The normalized neural net (NN1) output for the two sets of cosmic ray air shower simulation (weighted as dotted crosses, unweighted as triangles), the experiment and the UHE neutrino induced events.

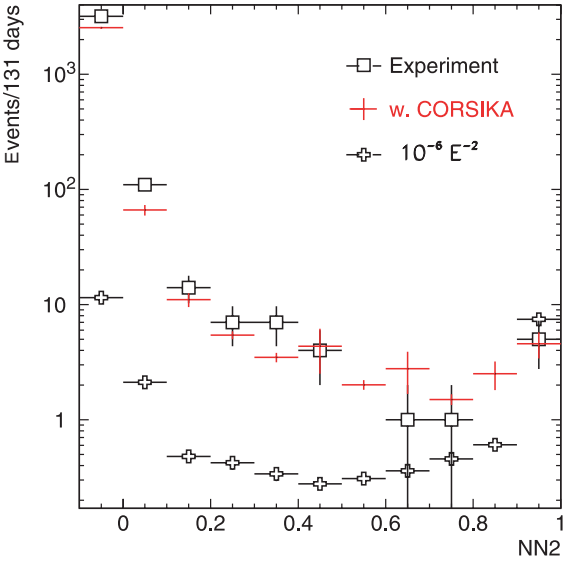

Fig. 7. The experimental data and the prediction from the air shower simulation for the neural net NN2. The number of events expected from an $10^{-6}E^{-2}\mathrm{GeV\,cm^{-2}\,s^{-1}\,sr^{-1}}$ neutrino source (all flavors equally mixed) is superimposed.

4.4. The final selection criterion and sensitivity

The final selection criterion is based on the output of the neural net NN2. To find the criterion that puts the strongest constraint on a given theoretical model the procedure outlined by Hill and Rawlins [21] is used. This method uses only information from Monte-Carlo simulations and is therefore free from bias introduced by using experimental data. The simulated background expectation n_b as a function of the selection variable is used to calculate the average event upper limit $\overline{\mu}_{90}$ (90% confidence limit) as defined in [22]. The strongest constraint on a theoretical model corresponds to the selection criterion that minimizes the model rejection factor $\overline{\mu}_{90}/n_s$ where n_s is the number of events expected from this model that satisfy the selection criteria. The average flux upper limit, or sensitivity, is defined as $\overline{\Phi}_{90} = \Phi\frac{\overline{\mu}_{90}}{n_s}$, where Φ is the neutrino flux predicted by a specific theoretical model. The model rejection factor states how strongly, on average, a given flux Φ is rejected when performing repeated (hypothetical) runs of the experiment. The actual experiment will obtain a limit based on the observed number of events. Fig. 8 shows the model rejection factor for an $E^2\Phi = 10^{-6}\,\mathrm{GeV\,cm^{-2}\,s^{-1}\,sr^{-1}}$ neutrino flux. As the neural net assigns signal-like events values close to one, it is expected that the largest rejection power is achieved for a selection close to this value. Indeed, the inset in Fig. 8, using finer binning, shows a minimum close to NN2 = 1. Here NN2 > 0.9 is chosen, ignoring the loss of approximately 10% in rejection power compared to the actual minimum. For this selection, $n_s = 7.44 \pm 0.14$ and $n_b = 4.6 \pm 1.2$ is expected from simulations for signal and background, respectively. This results in a sensitivity of 5.1 events (90% confidence level), or $E^2\overline{\Phi}_{90}(\nu_e : \nu_\mu : \nu_\tau = 1:1:1) = 0.69\times 10^{-6}\,\mathrm{GeV\,cm^{-2}\,s^{-1}\,sr^{-1}}$. At this level, by calculating the number of equivalent events, the biased Monte Carlo background simulation corresponds to approximately 3 times the experimental live time.

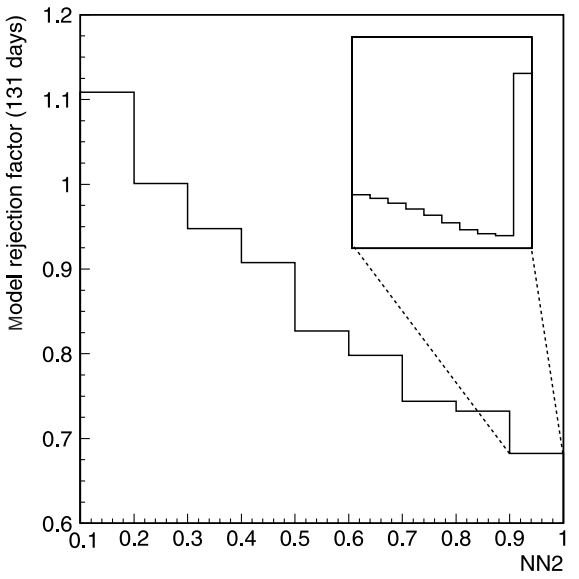

Fig. 8. The model rejection factor for an $E^2\Phi = 10^{-6}\,\mathrm{GeV\,cm^{-2}\,s^{-1}\,sr^{-1}}$ neutrino flux. The x-axis denotes the selection with NN2 larger than the corresponding value. Selecting events with NN2 > 0.9 leads to a model rejection factor of 0.69.

4.5. Effective detector area

The effective area for neutrinos, A_{eff}, represents the area of an ideal detector capable of detecting neutrinos with full efficiency. Using the effective area for neutrinos one can calculate neutrino induced event rates for a given neutrino flux. The number of events is calculated by:

$$N_{\mathrm{event}} = T\int \mathrm{d}E_\nu \mathrm{d}\Omega\Phi(E_\nu,\Theta_\nu)A_{\mathrm{eff}}(E_\nu,\Theta_\nu).$$

With T the live time of the experiment, E_ν and Θ_ν denote the energy and the zenith angle of the neutrino. Fig. 9(left) shows the effective area for neutrinos as a function of energy for the three flavors averaged over the azimuth and zenith angles. As the energy increases the muon–neutrino contribution dominates over those from electron– and tau–neutrinos, because of the increasing path length of the muons. At 10^{11} GeV the detector is approximately 4–5 times more sensitive for muon–neutrinos than for electron–neutrinos, the sensitivity for tau–neutrinos being in-between. Due to the angular averaging, this figure implicitly averages the effects of absorption and interaction probability. Fig. 9(right) shows that for nearly

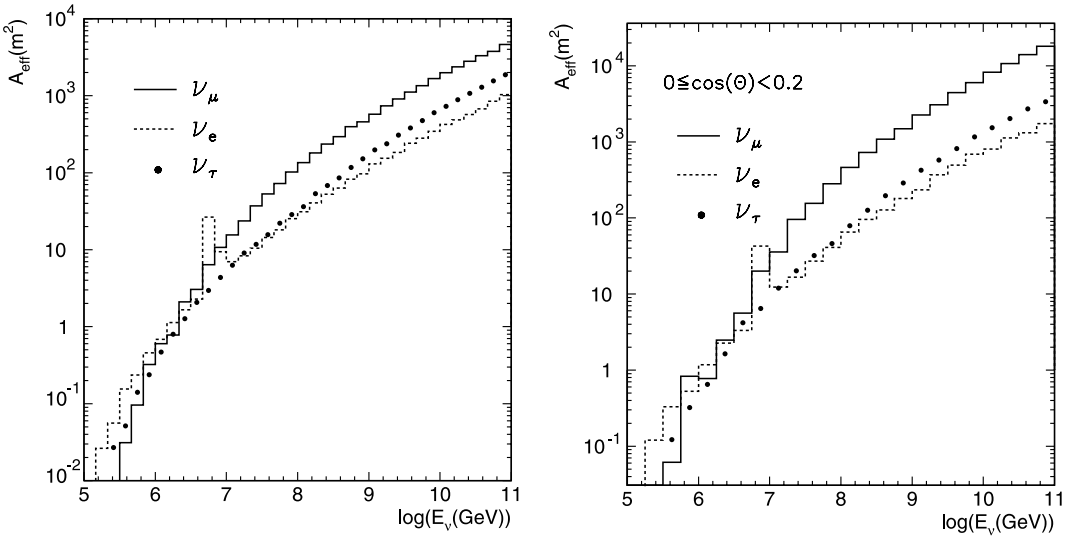

Fig. 9. The effective area for neutrinos of all three flavors averaged over all angles (left) and for nearly horizontal events (right).

Table 2
Event rates (Hz) for the different analysis levels for the experiment and the background simulation performed with CORSIKA

	Selection criteria			
	NCH > 95	F1H < 0.65	NN1 > 0.37	NN2 > 0.9
Experiment	0.35	0.023	2.9×10^{-4}	4.4×10^{-7}
CORSIKA	0.31	0.026	2.6×10^{-4}	4.1×10^{-7}

horizontal events, the detection area is much larger than the averaged area and exceeds $10^4\,m^2$ for horizontal muon–neutrinos.

4.6. Event rates

The overall absolute sensitivity of the simulation is verified by comparing the predicted event rate from background simulations with the experimental rate. Table 2 shows the event rates for the different selection criteria. The number of experimental events drops from 4×10^6 to 5 and the simulated background rate describes the experimental rate at all levels within the systematic uncertainties.

5. Systematic uncertainties

Systematic uncertainties in simulation input parameters lead to an uncertainty in the final result. Changes in these parameters influence the number of expected signal or background events for a fixed set of selection criteria. In this analysis the main uncertainties are related to the properties of the ice as medium for photon propagation, the muon propagation in the ice, the absolute detector sensitivity, the neutrino cross section at high energies and the absolute flux and composition of the primary cosmic rays. The effects of variations in the simulation input parameters on the number of events remaining after the final selection are studied. The derived systematic uncertainties are included in the limit calculation using the method of Conrad et al. [23], which is an extension of the approach of Cousins and Highland [24].

5.1. Absolute detector sensitivity

There are three main uncertainties affecting the absolute sensitivity of the detector: the absolute

sensitivity of the OMs, the shadowing of the OMs by the string-cable, and the effect of the exact optical properties of the re-frozen ice enclosing the OMs in the 60 cm wide drill hole. The determination of the uncertainty in the absolute sensitivity of the OM cannot easily be decoupled from the uncertainty in the ice properties. Following the discussion in [25] the uncertainty in the absolute sensitivity of the OM is estimated to be 15%.

5.2. Optical ice parameters

High energy muons generate a large number of photons in the ice. These photons are scattered and absorbed. Due to the large number of photons, some photons can be detected over long distances in the ice. This analysis uses an average effective scattering and absorption length ($\lambda_{\text{eff}} = 24\,\text{m}$, $\lambda_{\text{abs}} = 130\,\text{m}$) to describe the propagation of photons. The error on both parameters is estimated to be about 10%. The parameters are not independent, i.e. a larger scattering length implies a larger absorption length. To estimate the systematic effect, we simulate the muon–neutrino signal with ($\lambda_{\text{eff}} = 19\,\text{m}$, $\lambda_{\text{abs}} = 90\,\text{m}$), ($\lambda_{\text{eff}} = 22\,\text{m}$, $\lambda_{\text{abs}} = 110\,\text{m}$) and ($\lambda_{\text{eff}} = 26\,\text{m}$, $\lambda_{\text{abs}} = 145\,\text{m}$) in addition to the standard combination. The variation of the parameters span a wider range than allowed by the estimated uncertainty, to account for an overall shift seen in these values when comparing earlier [1] and newer analyses [26] of experimental data. The variation of the ice parameters changes the absolute number of events predicted by the simulation. If the number of events predicted by the simulation were to differ from the number of observed events by significantly more than allowed by the overall error one would introduce a normalization procedure. This is taken into account when determining the systematic uncertainty due to variation of the optical parameters, by normalizing the number of events in the leftmost (most background like) bin in the NN2 distribution arbitrarily to 100. Using Table 3, the relative error of the average number of events, 34%, is taken as systematic uncertainty introduced by the uncertainty in the description of the optical properties of the ice.

Table 3
Number of events passing the final selection criterion NN2 > 0.9 for different combinations of effective scattering and absorption length

Ice model	Events passing NN2 > 0.9
$\lambda_{\text{eff}} = 19\,\text{m}$, $\lambda_{\text{abs}} = 90\,\text{m}$	22.2
$\lambda_{\text{eff}} = 22\,\text{m}$, $\lambda_{\text{abs}} = 110\,\text{m}$	26.7
$\lambda_{\text{eff}} = 24\,\text{m}$, $\lambda_{\text{abs}} = 130\,\text{m}$	22.7
$\lambda_{\text{eff}} = 26\,\text{m}$, $\lambda_{\text{abs}} = 145\,\text{m}$	42.7
Average	28.6 ± 9.6
Relative error	34%

The relative difference in event numbers is an estimate of the systematic error introduced by uncertainties in the description of the optical ice properties.

5.3. Muon propagation

The path length and energy loss distribution for muons during their passage through ice is subject to uncertainties. To investigate this effect, muons caused by UHE neutrinos are propagated with two different muon propagation codes [19,18] and the number of signal events passing the final selection NN2 > 0.9 are counted. From this, the uncertainty related to muon propagation simulation is estimated to be 6%.

5.4. Neutrino cross section

In [27] neutrino cross sections are calculated up to $10^{21}\,\text{eV}$. Below $10^{16}\,\text{eV}$ all standard sets of parton distributions yield very similar cross sections. Above this energy, the cross sections are sensitive to assumptions made about the behavior for $x \to 0$. The authors of [27] conclude that at $10^{20}\,\text{eV}$ the uncertainty reaches a factor of 2. Here the charged-current cross section is multiplied/divided by a factor that increases linearly to 2 with the energy increasing from $10^{16}\,\text{eV}$ to $10^{20}\,\text{eV}$. Again, the number of signal events passing the final selection NN2 > 0.9 is counted and an uncertainty of 8% is derived.

5.5. Primary cosmic ray flux

The uncertainty in the absolute primary cosmic ray flux enters as a scaling factor for the number of events expected from atmospheric air shower

simulations. Ref. [28] summarizes the integrated flux averaged for different experiments and gives the spread between the data from different experiments as error. In the energy range of interest the error on the absolute flux does not exceed 20%. Different elements of the same energy as primary cosmic ray particles lead to a different shower development and can affect the number of events expected from these air showers. The model used for the primary cosmic ray composition taken from [17] is shown in Fig. 3. This model fits a "heavy" composition for high energy primaries. Using data from the combined SPASE-AMANDA experiment, a similar trend to heavier primaries at higher energies is seen [29]. To investigate the sensitivity of the analysis to the composition of the primary cosmic rays, the proton and iron content was varied between 0% and 100%. The two extremes, protons only or iron only, together with the model from Fig. 3 are shown at Level 2 in Fig. 10. The shape of the distribution is not influenced by the primary composition. After normalizing to the number of events in experimental data (3326 events), the variation in the number of events passing the NN2 > 0.9 selection while varying the proton/iron content is used to determine the uncertainty. Allowing the two extremes (proton or iron only) this uncertainty is about 25%. This is an overestimation, as the proton or iron only compositions are contradicted by other experiments. Allowing a minimum of 20% of protons or iron as extremes decreases the uncertainty to about 15%, the value used in this analysis.

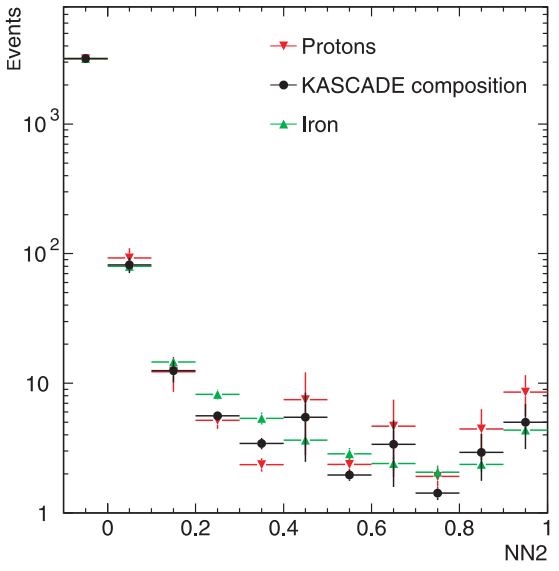

Fig. 10. NN2 for cosmic ray air shower simulations and different primary compositions at Level 2. The composition from [17] is also shown in Fig. 3, the other two represent the extreme cases of only proton or iron primaries. The total number of events is normalized to the experimental number of events.

5.6. Summary of systematic uncertainties

This analysis accounts for the major sources of systematic uncertainties, including uncertainties in the background simulation. The variation of the optical properties leads to the largest error of 34%, the absolute sensitivity of the OM contributes 15%, the neutrino cross section 8% and the muon propagation 6%. Treating these errors as independent and adding them quadratically, the signal uncertainty becomes 39%. For down-going atmospheric air showers (i.e. background), we add in quadrature the statistical uncertainty of 26% (4.6 ± 1.2 expected events), uncertainties from composition of 15% and normalization of the absolute flux of 20% yielding a total uncertainty of 36%.

6. Neutrino flux limits

Fig. 7 shows the distribution of NN2 for experimental data, the simulated air showers, and a neutrino flux simulation with $E^2\Phi = 10^{-6}\,\mathrm{GeV\,cm^{-2}\,s^{-1}\,sr^{-1}}$. Applying the selection criterion NN2 > 0.9, the simulation gives a background expectation of 4.6 ± 1.2 events while the experiment yields 5 events for a live time of 131 days. Using the tables by Feldman and Cousins [22] and disregarding systematic uncertainties, this results in an upper limit of 4.7 events at 90% confidence level. With this, an all flavor neutrino source with a spectrum proportional to E^{-2} is limited by $E^2\Phi = 0.63 \times 10^{-6}\,\mathrm{GeV\,cm^{-2}\,s^{-1}\,sr^{-1}}$. Including the systematic uncertainties as evaluated above and following the method described in [23], the event upper limit increases to 7.35 (90% confi-

dence level) and the upper flux limit to $E^2\Phi = 0.99 \times 10^{-6}\,\mathrm{GeV\,cm^{-2}\,s^{-1}\,sr^{-1}}$. This is 57% above the limit without systematic uncertainties. Fig. 11 shows the energy distribution for a diffuse neutrino flux corresponding to the above limit. Ninety percent of the events are contained in the energy region from 10^{15} eV to 3×10^{18} eV, with peaks just above 10^{16} eV for the muon–neutrino contribution and at the Glashow resonance (6.3 PeV) for the electron–neutrino contribution.

The experimental data can be used to set limits on neutrino flux predictions other than a generic E^{-2} spectrum. Several AGN models in the literature predict fluxes that might be detectable with the sensitivity derived above. The pioneering AGN core model by Stecker et al. (S91) [30] has been updated by the more recent model (S96) [31]. Others are the AGN jet model by Protheroe (P97) [32] and a model by Mannheim (M95) [33]. With systematic uncertainties included, this analysis excludes at 90% confidence level the neutrino fluxes predicted by the models S91, S96 and P97 with model rejection factors between 0.24 and 0.97, while M95 is not quite excluded (see Table 4). Other models generally predict lower fluxes, while neutrinos from cosmic ray interactions with

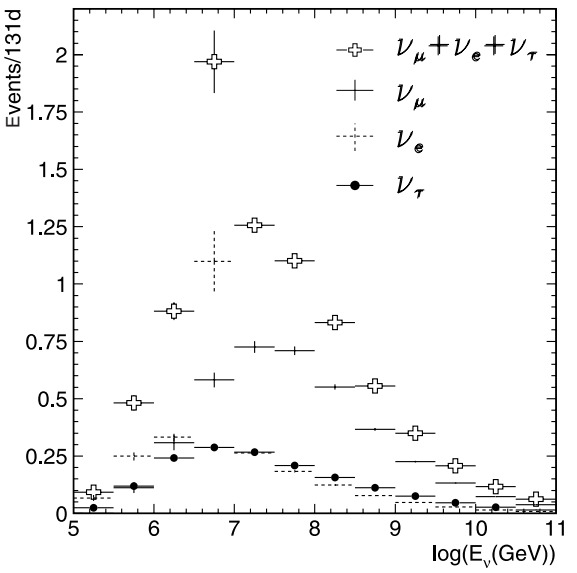

Fig. 11. Energy distribution for the sum and the individual contributions of the three neutrino flavors for a diffuse E^{-2} neutrino flux with a strength of $E^2\Phi = 0.99 \times 10^{-6}$ $\mathrm{GeV\,cm^{-2}\,s^{-1}\,sr^{-1}}$ after the final selection criterion. The number of events from ν_e, ν_μ and ν_τ are 2.2, 3.6 and 1.5.

Table 4
Number of events expected (n_s) for 131 days after applying the selection NN2 > 0.9 for a generic E^{-2} source and four different predicted AGN models (references given in the text)

Model	n_s NN2 > 0.9	$\overline{\mathrm{mrf}}$	mrf excl. sys.	mrf incl. sys.
$10^{-6}E^{-2}$	7.44 ± 0.14	0.69	0.63	0.99
S91	7.56 ± 0.25	0.67	0.62	0.97
S96	30.5 ± 1.0	0.17	0.15	0.24
P97	13.45 ± 0.21	0.38	0.35	0.55
M95	6.17 ± 0.04	0.83	0.76	1.19
UL	–	5.1	4.7	7.35

The model rejection factor is the factor by which the source strength needs to be multiplied to equal the event upper limit (UL). The middle column ($\overline{\mathrm{mrf}}$) gives the sensitivity, while the last two columns give the experimental results for the model rejection factor excluding and including systematic uncertainties. A rejection factor <1 indicates an exclusion of the neutrino flux caused by the model at 90% confidence level.

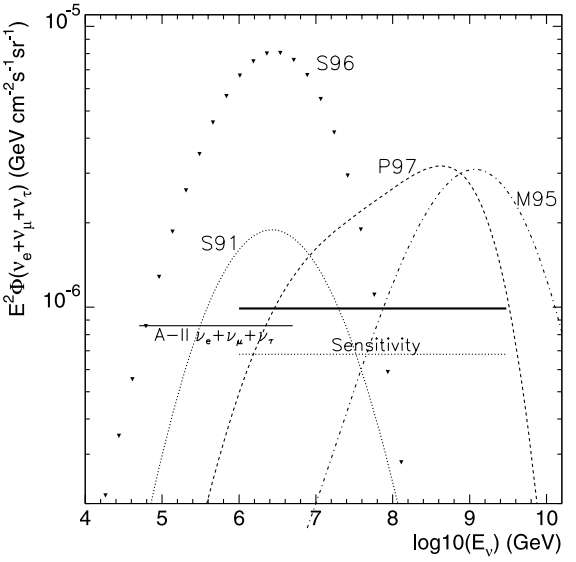

Fig. 12. Three models of AGN neutrino emission, S91 [30], S96 [31] and P97 [32] which are excluded by this analysis and the not quite excluded model M95 [33] are shown as well as the experimental 90% confidence level upper limit to an diffuse E^{-2} all flavor neutrino flux as a bold solid line. The dotted line shows the sensitivity of this analysis. The thin line to the left shows the AMANDA-II all flavor limit [35] for lower energies. The range of the presented limit corresponds to the region that contains 90% of the expected signal.

the microwave background or from decays of topological defects are too high in energy and too low in flux for the achieved sensitivity.

7. Summary and discussion

Data recorded with the AMANDA-B10 detector in 1997 are searched for leptons caused by a diffuse flux of UHE neutrinos. In contrast to the analyses [26] and [34] which used the AMANDA detector to search for an upward traveling flux of neutrinos, or the analysis [35] which optimized for cascades at lower energies, this analysis searches for a UHE signal from horizontal and down-going events. Restricting the analysis to very bright events, the flux of down-going muons caused by atmospheric air showers can be sufficiently suppressed while retaining a large sensitivity to neutrinos. At all levels, the experimental data are described well by the air shower simulation. The sensitivity (excluding systematic errors) of this analysis to an equally mixed all flavor neutrino flux is $E^2\overline{\Phi} = 0.69 \times 10^{-6}\,\mathrm{GeV\,cm^{-2}\,s^{-1}\,sr^{-1}}$. Including a combined error (statistical and systematic) of 36% for the background and 39% for the signal simulation, this analysis sets a flux upper limit for 131 days of $E^2\Phi(\nu_e{:}\nu_\mu{:}\nu_\tau = 1{:}1{:}1) = 0.99 \times 10^{-6}\,\mathrm{GeV\,cm^{-2}\,s^{-1}\,sr^{-1}}$ at 90% confidence level, shown as bold line in Fig. 12. The energy range 10^{15}–3×10^{18} eV contains 90% of the neutrino induced events, with the remainder being equally divided above and below this range. This energy range is well suited to exploring neutrino emission models from AGN blazars, and three specific model predictions, two by Stecker et al. [30,31] and one by Protheroe [32], are excluded. The recent analysis [35] has excluded the two models by Stecker et al., but not the model by Protheroe. An extension to even higher energies would be desirable in order to explore neutrino emission from the decay of topological defects or to search for the guaranteed UHE neutrinos from interactions of the highest energy cosmic rays with the

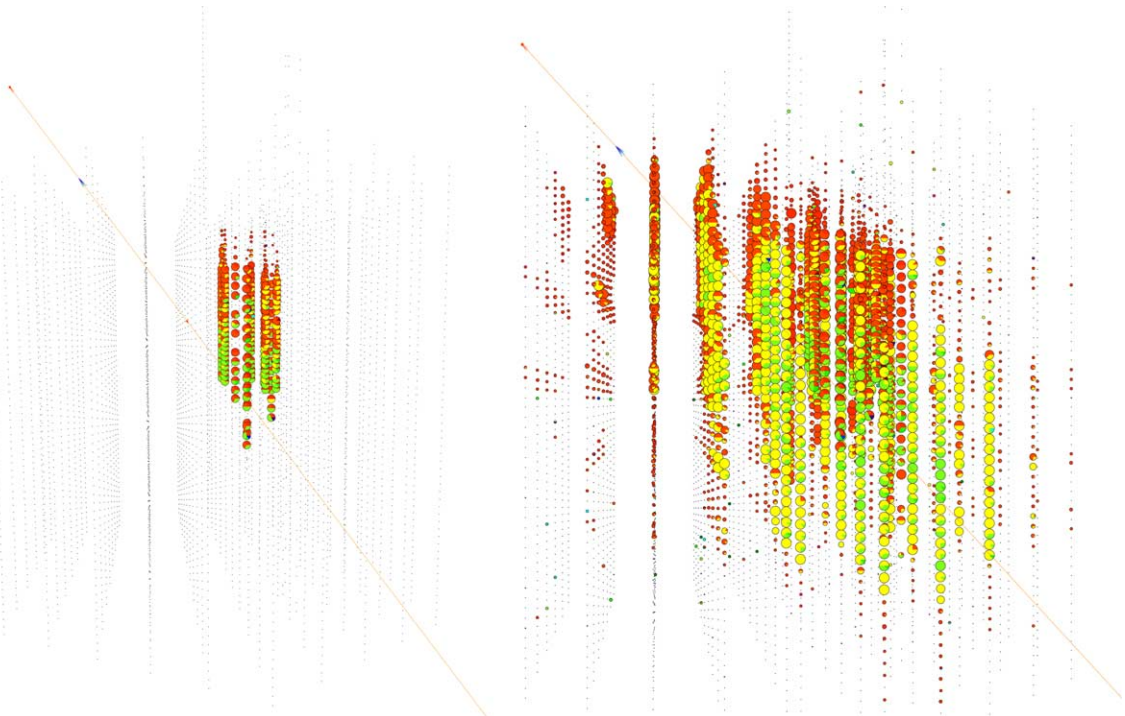

Fig. 13. The same UHE muon–neutrino event in the AMANDA-B10 detector (left) and the IceCube array (right), illustrating the amount of additional information gained by the larger size of the detector and the larger number of optical modules in IceCube.

microwave background radiation. This is prevented by the limited size and relatively small number of OMs of the AMANDA-B10 detector, where saturation effects become visible. However the larger AMANDA-II detector [36] equipped with optical fibers for dispersion free signal transmission and its advanced technique of waveform capture will improve the analysis of UHE neutrinos, as will the IceCube detector [37] on a longer time scale. Fig. 13 shows the simulated response to a muon caused by an UHE neutrino interaction passing the AMANDA-B10 and IceCube array, respectively. In particular the IceCube array, with construction beginning during 2004/2005, will dramatically increase the amount of information exploitable in the UHE regime.

Acknowledgements

We acknowledge the support of the following agencies: National Science Foundation—Office of Polar Programs, National Science Foundation—Physics Division, University of Wisconsin Alumni Research Foundation, Department of Energy and National Energy Research Scientific Computing Center (supported by the Office of Energy Research of the Department of Energy), UC-Irvine ANEAS Supercomputer Facility, USA; Swedish Research Council, Swedish Polar Research Secretariat and Knut and Alice Wallenberg Foundation, Sweden; German Ministry for Education and Research, Deutsche Forschungsgemeinschaft (DFG), Germany; Fund for Scientific Research (FNRS-FWO), Flanderns Institute to encourage Scientific and Technological Research in Industry (IWT) and Belgian Federal Office for Scientific, Technical and Cultural affairs (OSTC), Belgium; Fundación Venezolana de Promoción al Investigador (FVPI), Venezuela; D.F.C acknowledges the support of the NSF Career program; E.R. acknowledges the support of the Marie-Currie fellowship program of the European Union.

References

[1] E. Andres et al. [AMANDA Collaboration], Nature 410 (2001) 441.
[2] R. Gandhi et al., Phys. Rev. D 58 (1998) 093009.
[3] J.R. Klein, A.K. Mann, Astropart. Phys. 10 (1999) 321.
[4] S. Hundertmark et al. [AMANDA Collaboration], Proc. 27th Int. Cosmic Ray Conf., Hamburg, Germany (2001) 1129.
[5] E. Waxman, Nucl. Phys. Proc. Suppl. 100 (2001) 314.
[6] J.G. Learned, K. Mannheim, Ann. Rev. Nucl. Part. Sci. 50 (2000) 679.
[7] R.J. Protheroe, arXiv:astro-ph/9612213.
[8] H. Athar et al., Phys. Rev. D 62 (2000) 103007.
[9] L. Anchordoqui et al., arXiv:hep-ph/0407020.
[10] S. Hundertmark et al. [AMANDA Collaboration], DESY-PROC-2002-01, 2002, 69.
[11] Photonis, Photomultiplier tubes, http://www.photonis.com.
[12] Hamamatsu, Photomultiplier Tubes, Basics and Applications, second ed., 1999.
[13] M. Kowalski and A. Gazizov, arXiv:astro-ph/0312202.
[14] A.M. Dziewonski, D.L. Anderson, Phys. Earth Planet. Interiors 25 (1981) 297.
[15] D. Heck, DESY-PROC-1999-01 (1999) 227.
[16] B. Wiebel-Sooth, P. Biermann, Landolt-Bornstein, vol. VI/3c, Springer Verlag, 1999, pp. 37–90.
[17] R. Glasstetter et al. [KASCADE Collaboration], FZKA-6345E (1999).
[18] D. Chirkin, W. Rhode, arXiv:hep-ph/0407075.
[19] P. Lipari, T. Stanev, Phys. Rev. D 44 (1991) 3543.
[20] J. Ahrens et al. [AMANDA Collaboration], Nucl. Instrum. Methods A 524 (2004) 169.
[21] G.C. Hill, K. Rawlins, Astropart. Phys. 19 (2003) 393.
[22] G.J. Feldman, R.D. Cousins, Phys. Rev. D 57 (1998) 3873.
[23] J. Conrad et al., Phys. Rev. D 67 (2003) 012002.
[24] R.D. Cousins, V.L. Highland, Nucl. Instrum. Methods A 320 (1992) 331.
[25] J. Ahrens et al. [AMANDA Collaboration], Astrophys. J. 583 (2003) 1040.
[26] J. Ahrens et al. [AMANDA Collaboration], Phys. Rev. Lett. 90 (2003) 251101.
[27] R. Gandhi et al., Astropart. Phys. 5 (1996) 81.
[28] J.R. Hoerandel, Astropart. Phys. 19 (2003) 193.
[29] T. Miller et al. [SPASE and AMANDA Collaborations], Astropart. Phys. 21 (2004) 565.
[30] F.W. Stecker et al., Phys. Rev. Lett. 66 (1991) 2697; F.W. Stecker et al., Phys. Rev. Lett. 69 (1992) 2738 (Erratum).
[31] F.W. Stecker, M.H. Salamon, Space Sci. Rev. 75 (1996) 341.
[32] R.J. Protheroe, arXiv:astro-ph/9607165.
[33] K. Mannheim, Astropart. Phys. 3 (1995) 295.
[34] J. Ahrens et al. [AMANDA Collaboration], Phys. Rev. D 67 (2003) 012003.
[35] M. Ackermann et al. [AMANDA Collaboration], Astropart. Phys. 22 (2004) 127.
[36] S.W. Barwick et al. [AMANDA Collaboration], arXiv:astro-ph/0211269.
[37] IceCube Project web page, http://icecube.wisc.edu.